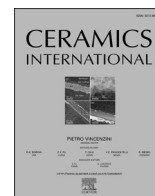


Contents lists available at [ScienceDirect](https://www.sciencedirect.com)

Ceramics International

journal homepage: [www.elsevier.com/locate/ceramint](https://www.elsevier.com/locate/ceramint)

# Optimization of structural and electrical properties of graphene-based TiO<sub>2</sub> thin film device using Bayesian machine-learning approach

Hud Wahab<sup>a</sup>, Jacob Heil<sup>a</sup>, Alexander Scott Tyrrell<sup>a</sup>, Todd Muller<sup>a</sup>, John Ackerman<sup>a</sup>, Lars Kotthoff<sup>a</sup>, Patrick A. Johnson<sup>b,\*</sup>

<sup>a</sup> Department of Chemical and Biomedical Engineering, University of Wyoming, 1000 E University Avenue, 82071 Laramie, WY, USA

<sup>b</sup> Department of Materials Science and Engineering, Iowa State University, 2240 Hoover Hall 528 Bissell Road, Ames, IA 50011, USA

## ARTICLE INFO

Handling Editor: Dr. P. Vincenzini

### Keywords:

Machine learning  
Bayesian optimization  
Laser-induced graphene  
Titanium dioxide  
Negative capacitance

## ABSTRACT

The optimization of laser-induced graphene (LIG) patterning is crucial for achieving desirable electronic properties in flexible electronic devices. In this study, we applied state-of-the-art automated parameter optimization techniques, specifically Bayesian optimization, to enhance the electrical resistance of LIG patterns. By iteratively optimizing the laser power, irradiation time, pressure, and gas type, we achieved minimum LIG resistance within eight batch configurations suggested by the Bayesian optimization (BO) approach. Our method eliminates the reliance on skilled operators, as the initial surrogate models were trained with random parameter evaluations. Notably, our system enables the optimization of material properties even when characterizations are only available outside the experiment loop. Furthermore, the surrogate model provided insights into the underlying mechanisms of LIG growth on quartz substrates. Through partial dependence analysis, we identified relevant physical domains for further investigation, leading to the discovery of negative capacitance and a correlation between structural and electrical properties in LIG. These findings were supported by XPS, Raman, and optical characterizations. Our approach streamlines the experimental design, reducing time and cost while accelerating materials research, and offers human-interpretable conclusions for a deeper understanding of LIG patterning processes.

## 1. Introduction

Laser-induced graphene (LIG) has shown potential in fabricating flexible electronic devices [1]. Following the discovery of LIG, precise control over its physical, chemical and electronic properties would allow one to broaden the scope of its applications to new areas such as micro-supercapacitors [2,3] and fuel cell technology [4]. Therefore, there is considerable interest in advancing strategies for property engineering of LIG; in particular, optimizing the lasing parameters and the local environment for different substrates allows to control its composition and morphology.

Optimization studies aim to find optimal configurations by optimizing an objective function based on a set of parameters. Grid search is a commonly used strategy where the parameter space is divided into a grid and sampled for evaluation. While grid search works well for experimental design, it becomes inefficient when dealing with real-valued and dependent parameters in higher dimensions. Traditional

approaches like the Taguchi method and the Fisher method rely on predefined grids or discrete parameter values, respectively, which may overlook important features of the objective landscape. These strategies often require a large number of experiments or computations to adequately sample the grid, making them unsuitable for optimization studies with expensive objective function evaluations [5–7].

The optimization of laser reduction parameters in LIG fabrication is typically performed through manual trial and error, as exhaustive grid searches are infeasible. The efficiency and outcome of the optimization process often depend on the expertise of the individual conducting it. Bayesian optimization (BO) is a state-of-the-art machine learning (ML) approach that is well established in solving such parameter optimization problems [8–10]. BO employs surrogate models to estimate the performance of different hyperparameter configurations, iteratively selecting configurations that are predicted to yield the best results while considering both the model's predictions and uncertainty.

State-of-the-art techniques in materials informatics have primarily

\* Corresponding author.

E-mail address: [paj3@iastate.edu](mailto:paj3@iastate.edu) (P.A. Johnson).

<https://doi.org/10.1016/j.ceramint.2023.12.225>

Received 11 September 2023; Received in revised form 7 December 2023; Accepted 16 December 2023

Available online 23 December 2023

0272-8842/© 2024 Elsevier Ltd and Techna Group S.r.l. All rights reserved.

focused on leveraging large databases of computational work to accelerate the discovery of new materials [11–14]. To optimize the properties of a new material, extensive parameter studies are often required. Some research groups have reported successful implementation of closed-loop experimental work, where ML models were sequentially updated with new measurements [15–17]. These studies follow a general Bayesian optimization approach, enabling the optimization of LIG patterning conditions with a minimal number of iterations.

The iterative and adaptive approach can streamline the optimization of LIG patterning conditions. Automated parameter tuning techniques, specifically Bayesian optimization aim to find the best parameter configuration for a given application by iteratively predicting and evaluating different configurations [18]. Surrogate models are utilized to efficiently explore the parameter space and identify promising configurations for further evaluation [18,19]. With the BO approach, one might argue that accurate predictions are not even necessary as long as promising regions of the parameter space are progressively identified in subsequent iterations.

In this study, we describe BO-assisted fabrication of a graphene-based capacitor using laser-induced graphene and a  $\text{TiO}_2$  dielectric. We discovered experimental conditions that lead to LIG patterns with electrical performance comparable to literature, and deduced the electrical-structural correlation of LIG. We then demonstrate the human interpretability of the model that gives insight into the LIG processing conditions. Additionally, we report the indirect occurrence of negative capacitance, which, when exploited, could compensate for parasitic capacitances, reduce power consumption, and extend the operational bandwidth of advanced electronic devices [20]. Since the BO approach presented here suggests promising configurations iteratively, we consider this work an initial step in the development of human-in-the-loop automated LIG patterning and characterization systems.

## 2. Experimental setup and methods

### 2.1. Synthesis of multi-layered thin films

Briefly, we describe here the synthesis of each layer in our capacitive device, namely laser-induced graphene (LIG) bottom and top electrodes and the  $\text{TiO}_2$  insulating layer.

#### 2.1.1. Bottom- and top-layer graphene

Graphene oxide (GO) was synthesized from graphite using the improved Hummers' method [21] and processed into GO thin films that were deposited on a quartz substrate via ultrasonic spray deposition, as previously described [22]. The appropriate thickness of GO to use in the device was determined based on the upper limits of the reactor temperature during  $\text{TiO}_2$  deposition; GO films thicker than 300 nm resulted

in local film expansion when annealed up to 450 °C (see Fig. S1). Therefore, GO thickness of 250 nm was deposited and verified by scratching the surface and measuring the height using an optical profilometer (VK-X1000, Keyence). The samples were stored in a closed container in a vacuum desiccator, and taken out in ambient air at a maximum of a day between layer depositions and characterizations.

The LIG lines were patterned via a fully automated one-step laser direct-writing process on the deposited GO thin film. The lines were patterned using lasing and environmental parameters that were optimized using a Bayesian optimization approach, which is further elaborated in Section 2.3. In particular, the parameters were chosen at the minimum electrical resistance of the LIG line, given the spatial constraints of the sample. The sample area is 1  $\text{cm}^2$ , which allows patterning a total of 14 lines at the bottom GO layer (Fig. 1a); the lines are 2 mm in length, where constant speed is maintained throughout. For the device, two identical LIG lines were patterned across the bottom layer (Fig. 1b); the lines at the top GO layer is limited to 12 lines to allow for silver pad contacts (Fig. 1d, V-One, Voltera) for the two-point probe measurements. The capacitive area where the top and bottom LIG layer overlaps is about 2500  $\mu\text{m}^2$  (Fig. S2).

#### 2.1.2. $\text{TiO}_2$ layer

Titanium dioxide ( $\text{TiO}_2$ ) films were prepared via chemical vapor deposition (CVD) from a titanium ethoxide precursor. Following the preparation of bottom LIG electrodes (Fig. 1c), the samples were placed in the reactor for 45 min along with a silicon standard as a visual guide for  $\text{TiO}_2$  thickness. The main heating element was set to 410 °C and auxiliary plumbing was also kept heated to prevent condensation of reactants. The precursor was vaporized at 140–142 °C, and a  $\sim 10^{-5}$   $\text{mol}/\text{cm}^3$  flow through the reactor was generated using a vacuum pump at pressures of 120–150 mTorr. The samples were allowed to cool in air for approximately 30 min. The thickness of the  $\text{TiO}_2$  films was deposited consistently at about 270 nm, verified by ellipsometry at normal incidence (Filmetrics F20, San Diego) for an average deposition rate of 90 Å/min.

### 2.2. Structural and electrical characterizations

The quality of the laser-induced graphene (LIG) lines was determined using Raman spectroscopy (532 nm, IsoPlane SCT320, Princeton Instruments), namely from G, D, 2D bands characteristic of carbon-based materials [23,24]. Additionally, we consider a broad feature D1 (also known as D'-band [25], or D"-band [26]) between the D- and G-bands, which has been reported in the Raman analysis of carbon-based materials [27–29]. Others have reported a full deconvolution of the Raman spectrum between 1100  $\text{cm}^{-1}$  – 1800  $\text{cm}^{-1}$ , including the D4 (or D\*)-band ( $\sim 1175 \text{ cm}^{-1}$ ) and the D2 (or D')-band ( $\sim 1620 \text{ cm}^{-1}$ ) [26,30]. However, when we reproduced their analysis on our patterned samples,

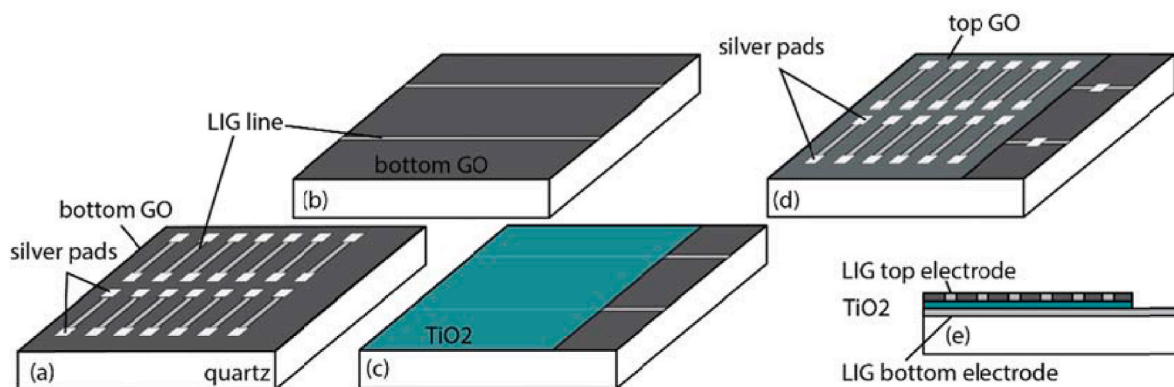


**Fig. 1.** Schematic of the graphene-based  $\text{TiO}_2$  capacitive device. (a) The batch of laser-induced graphene (LIG) lines used for Bayesian optimizations; (b) the LIG lines for the bottom electrodes; (c) deposition of the  $\text{TiO}_2$  insulating layer; (d) the LIG lines for the top electrodes; (e) Side-view of the layers in the device.

we found these peaks highly convoluted and the fits gave undesirably high uncertainties. Therefore, we have limited the fits to three peaks (Fig. 3) to avoid the risk of overfitting. The pre-, post-processing and fitting of Raman data are outlined in more detail in our previous work [31]. Additional Raman 2D maps of the electrode intersection were performed on an  $18 \times 11$  grid using a Gaussian-based interpolation [32].

An X-ray Photoelectron Spectrometer (XPS, Kratos AXIS SUPRA) with an Al-K $\alpha$  source and a charge neutralizer, was used to detect the changes of the C1s, O1s and Ti2p binding energies in the samples. All the XPS spectra were calibrated to the C1s adventitious carbon peak at 284.8 eV, following robust standards [33]. A standard Shirley background is used for all sample spectra shown in this work. XPS spectra were fitted with a least-squares Levenberg-Marquardt algorithm. Pseudo-Voigt functions were used to account for the asymmetric line shapes where necessary [44]. The C1s peaks were fit using general fitting parameters for graphitic, graphene, and carbon nanotube type materials [33].

For the electrical measurements, we quantified the conductivity of the induced graphene by uniformly printing silver contacts (Voltera V-One, Ontario) at the ends of each line and measuring the electrical resistance with a two-point probe. The silver prints contact were chosen instead of direct contact with the LIG line, as the former allows for a more stable contact resistance, which guarantees a linear relationship between the two point-contact resistance and the probe separation [34]; a uniform load is also applied on the contacts for consistent resistance measurements. Results were averaged over nine individual measurements. We note that these measurements are only possible by removing the sample from the reaction chamber, i.e. after 14 lines have been patterned, as removing and replacing the sample after each line is too much human effort to be feasible in practice (in particular realigning the sample would be a very time-consuming task). This means that the results of an experimental evaluation are only available after a complete batch has been evaluated. The capacitance was determined by measuring the impedance with an LCR precision meter (7600 Plus Precision, IET Labs).

### 2.3. Batch optimizations

An existing challenge to advance materials sciences is the physical disconnect that exists among the stages of synthesis, characterizations from multiple systems, and performance evaluations. In this study, even though the laser synthesis and structural characterization processes are automated, the automation of the process involving the extraction and reinsertion of the sample from the pressurized gas chamber for electrical characterization after each line necessitates an extensively customized robot arm. This arm must feature a range of specialized grippers and precision screw tools, a time- and cost-prohibitive endeavor that is impractical to achieve in most conventional materials science labs. Fortunately, the application of Bayesian batch optimization offers a promising solution to this challenge.

Batch optimization is qualitatively and fundamentally different to the original sequential BO formulation, where only one candidate is proposed per iteration, followed by the performance evaluation of that configuration; this optimal point can be definitively identified using all the available information from the acquisition function. In contrast, batch optimization proposes and evaluates multiple candidates simultaneously. Indeed, batch optimization avoids the need for sophisticated instruments and the trade-off is worth the savings in time and cost of experimentations.

We generated the batch proposals employing the constant liar technique [36]. The first point is chosen in the usual manner expected improvement is used to propose a single point, as previously demonstrated [22]. To obtain the second point, we make the assumption that the evaluation of the first point is complete. Since we lack an actual outcome at this stage, we attribute a fabricated value, i.e. a *lie*, to it. Typically, the best outcome is adopted as this fabricated *lie* value. This

fixed *lie* value is then used to update the model, thereby guiding the generation of subsequent points. This iterative process is repeated until the desired proposals are generated. The code snippet for the batch BO can be found in the Supplementary Information.

Choosing the Constant Liar (CL) method over alternatives like multi-acquisition functions is driven by several considerations. Firstly, multi-acquisition functions may propose the same point or very similar points because they leverage the same state of the surrogate model. In contrast, CL uses different surrogate models subsequently with each additional *lie*, i.e. the surrogate model is retrained on new data. Thus, CL avoids the risk of getting stuck at a local minimum. Secondly, the batch size can be limited to the number of acquisition functions available. Although in practice, a batch of 14 lines can be proposed by changing the parameters in the acquisition function (e.g.  $\lambda$ -parameter of upper/lower confidence bound). Lastly, CL facilitates reproducibility, providing a deterministic approach with a constant value. This enhances experiment reproducibility, simplifying result comparison and analysis across different runs.

The surrogate model was trained using the Gaussian process regression (GPR) package *regr.km* provided in the *mtr3* documentation with recommended hyperparameter configurations [35]. In contrast to other models e.g. random forest, they not only provide point estimates but also offer uncertainty quantification in the form of predictive variances. The benchmark for surrogate model performance comparing GPR to other models can be found in the Supplementary Fig. S3. Furthermore, the default covariance matrix *Matern(3/2)* captures the smoothness and correlations in the data. These configurations are especially valuable when dealing with experiments affected by noise, as it allows the domain expertise to make informed decisions while accounting for the inherent uncertainty in the data. To address noisy objectives, we modified the surrogate model. Instead of pure interpolation, we employed GPR to estimate the measurement error. This approach allows the Gaussian process to consider the measurement error, resulting in non-zero standard deviation predictions for the training data, reflecting the uncertainty in the observed function values due to measurement errors [36].

The experiments patterning lines had a total experimental budget of nine samples with 14 lines per sample, for a total of 126 lines. Despite the desire to minimize speculativeness by using fewer lines, we opted for 14 lines due to practical constraints. The physical limitations of the samples prepared and the high cost associated with each sample made it impractical to choose a smaller number of lines. One of the samples (14 parameter configurations) was used to evaluate configurations randomly sampled from the parameter space to train the initial surrogate model using the *constant liar* strategy [37]; The remaining eight samples were used to optimize the resistance of the patterned material. For the resistance measured for lines of graphene, we propose batches of 14 parameter settings to evaluate the surrogate model and is retrained for the next BO iteration after 14 such evaluations.

For the lines, we considered the following parameter space:

- The power range is limited to 10 mW–1190 mW to avoid damage to the sample we observed for high powers in some cases [22]. The precision was 10 mW and the step size 10 mW.
- The patterning speed was varied between  $0.267 \text{ mm s}^{-1}$  to  $1.905 \text{ mm s}^{-1}$ . This is dictated by the physical limits of the motor moving the sample chamber. The step size and precision were  $0.001 \text{ mm s}^{-1}$ .
- The pressure in the reaction chamber. The values for this parameter range from 60 psi to 350 psi, with a precision of 10 psi and a step size of 10 psi.
- The gas in the reaction chamber was limited to argon, based on results from irradiating spots where argon performed better [22].

These parameters give rise to a large space of possible combinations that is intractable to explore exhaustively. Data collection is expensive – running experiments is time-consuming and requires precursor

materials to be available. In contrast to big-data approaches, we need techniques that work with small amounts of data, such as the BO we apply here.

### 3. Results

#### 3.1. Layer-by-layer structural characterization

The Raman spectroscopy plot in Fig. 2 show peaks characteristic of crystalline graphene include the G- ( $\sim 1585\text{ cm}^{-1}$ ) and the 2D-bands ( $\sim 2700\text{ cm}^{-1}$ ), associated with the first- and second-order allowed Raman mode  $E_{2g}$ , respectively [38]; the D-band at  $\sim 1350\text{ cm}^{-1}$  appears when the basal plane structure of graphene is altered during graphite oxidation and the subsequent reduction of GO [39]. Compared to pristine graphene or graphite, some weak peaks centered between  $1100\text{ cm}^{-1}$  and  $1800\text{ cm}^{-1}$  were observed in GO flakes and powders [40,41]. Among these is the D1-band ( $\sim 1500\text{ cm}^{-1}$ ), which some authors have related to the vibrational density of states in graphite crystals of finite sizes [42]. S. Vollebregt et al. attributed the band to amorphous lattices after observing an inverse relationship of the decrease in D1-peak intensity with increase in crystallinity [25]. Other groups support the association of the D1-band with amorphous carbon fragments which may be functionalized small molecules at interstitial defects in  $sp^2$ -domains [27,29]. The mechanism of the existence of D1 is further outlined in Section 3.3.

The chemical states of Ti, O and C species and the interaction of graphene and  $\text{TiO}_2$  at the surface and interface of graphene/ $\text{TiO}_2$  were studied using XPS and Raman spectroscopy. Fig. 3 compares the Raman spectra of the quartz substrate and the GO, LIG,  $\text{TiO}_2/\text{GO}$  and  $\text{TiO}_2/\text{LIG}$  layers deposited on top. The prominent peaks associated with GO and LIG are observed at about  $1350\text{ cm}^{-1}$  and  $1590\text{ cm}^{-1}$ , corresponding to the D- and G-bands, respectively, as previously discussed. For the LIG layer, the increase in G/D ratio and presence of the 2D-band at about  $2700\text{ cm}^{-1}$  confirms graphitized structures. For the  $\text{TiO}_2/\text{GO}$  and  $\text{TiO}_2/\text{LIG}$  layers, we see the characteristic peaks of the anatase  $\text{TiO}_2$  phase; the intense peak at  $\sim 145\text{ cm}^{-1}$  is attributed to the main  $E_g$  anatase vibrational mode. Additionally, three vibration peaks at  $391\text{ cm}^{-1}$  ( $B_{1g}$ ),  $509\text{ cm}^{-1}$  ( $A_{1g}$ ) and  $645\text{ cm}^{-1}$  ( $E_g$ ) were observed (emphasized with dashed vertical lines), indicating that the anatase  $\text{TiO}_2$  crystallites were the major species [43]. Significantly, the peaks associated with GO and LIG structures were also observed for  $\text{TiO}_2/\text{GO}$  and  $\text{TiO}_2/\text{LIG}$ , respectively.

Interestingly, the  $\text{TiO}_2$  peaks are more obvious in  $\text{TiO}_2/\text{GO}$  than in  $\text{TiO}_2/\text{LIG}$ , as the quartz signals are well suppressed; a similar suppression is observed for the GO curve. This suggests that the Raman signal of  $\text{TiO}_2$  can be enhanced depending on the optical property of the underlying layers and substrate, as recently shown by others [44] and in

previous work [45]. Accordingly, when light passes through materials with variable refractive indices, it undergoes multiple reflections and interferences. In this case, the laser beam encounters the deposited layers and the underlying substrate, all with different refractive indices. In the visible range, GO has a comparable refractive index to the underlying quartz substrate ( $n \sim 1.5$ ), such that the reflection of GO dominates the total backscattered intensity [46]. In contrast, the refractive index of LIG ( $n \sim 2.5$ ) is higher than quartz [46], such that the quartz substrate reflects more strongly; consequently, LIG appears transparent in the visible wavelength region.

Further understanding of the electronic and chemical nature of the carbon/ $\text{TiO}_2$  interface was found in the layer-by-layer XPS measurements in Fig. 4. In Fig. 4a, the laser reduction in LIG shifts the C]C  $sp^2$  peak to lower binding energies by about  $0.1\text{ eV}$ , as seen by others [47, 48]. The structural shift between GO and LIG is also observed in the Raman spectra (Fig. 3). This occurs due to the laser reduction that restores the  $sp^2$  network and removes functional groups, as noted by others [49,50]. The restoration via laser reduction is further supported by observing CC- and CO-bonds; CC refers to the sum of C]C  $sp^2$  and C-C  $sp^3$  and the CO is the combination of C]O, C-OH and COOH groups. The ratio of the CC- to the CO bond (CC/CO) rises about three-fold from 1.9 (GO) to 5.7 (bottom LIG) and 6.3 (top LIG), which shows how oxygen functional groups were effectively removed from the GO substrate. Interestingly, even though our batch-optimized model was trained on minimizing electrical properties, the structural properties of LIG were also optimized; this supports how the two properties can be correlated, in particular, suggesting that the CC/CO can be used as a proxy to predict electrical properties of LIG or vice versa.

The effect of the  $\text{TiO}_2$  layer at the LIG/ $\text{TiO}_2$  interface is further investigated in the O1s and Ti2p binding energy regions in Fig. 4b and c, respectively. Without Ti, three oxygen species are fitted at  $530.1\text{ eV}$ ,  $531.8\text{ eV}$  and  $533.0\text{ eV}$ ; these are attributed to crystal lattice oxygen  $O_2$ , oxygen vacancy defects  $O_2, O_2^-, O^-$ ,  $CO_3^{2-}$  and, at least for graphene oxide GO, hydroxyl species OH- or surface-adsorbed water molecules ( $H_2O$ ), respectively [51]. The residual water molecules in GO illustrates its hydrophilic nature. For pure  $\text{TiO}_2$ , the determined binding energies of Ti2p $_{3/2}$  and Ti2p $_{1/2}$  are  $459.2\text{ eV}$  and  $465.1\text{ eV}$ , respectively, which agrees well with anatase  $\text{TiO}_2$  [52]. A slight shift in the Ti2p and O1s binding energies was observed, indicating a perturbation of the Ti and O electronic environment due to an electronic transformation at the same interface between LIG and  $\text{TiO}_2$ ; similarly, shifts observed for C]O from  $287.7\text{ eV}$  to  $287.9\text{ eV}$  and for COOH from  $288.8\text{ eV}$  to  $289.3\text{ eV}$ , are attributed to these transformations at the interface. Consequently, the  $E_g$  Raman mode of  $\text{TiO}_2$  at  $145\text{ cm}^{-1}$  has undergone a slight shift to higher wavenumbers upon its interaction with LIG. To be more precise, the Raman mode has shifted to  $150\text{ cm}^{-1}$ . It's important to note that this shift doesn't indicate a structural transformation from  $E_g$  in anatase to  $B_{1g}$  in rutile  $\text{TiO}_2$ , as such a shift would actually lead to a decrease in wavenumbers, not an increase [53]. Instead, these subtle shifts have been documented by others in cases where additional interfaces are present between different  $\text{TiO}_2$  facets and the graphene surface [54]. Therefore, XPS and Raman results confirm, that there is an electronic transformation at the LIG/ $\text{TiO}_2$  interface.

Furthermore, the small peak found at  $531.0\text{ eV}$ – $531.2\text{ eV}$  in the LIG/ $\text{TiO}_2$  and GO/ $\text{TiO}_2$  samples can be attributed to Ti–O–C bonds due to chemical interaction between metal oxide and graphene [55,56]. When comparing GO/ $\text{TiO}_2$  and LIG/ $\text{TiO}_2$  to GO and LIG, respectively, the relative peak ratios ( $O_{III}/O_I$ ) and ( $O_{II}/O_I$ ) have increased, which others have identified as hydroxylated surfaces that result in negatively charged oxygen vacancies [57,58].

#### 3.2. Batch optimization of electrical resistance

In Fig. 5a, the measured resistances for the lines patterned in batches are showcased. Notably, the optimized results exhibit improvement over the initial random data, albeit at a gradual pace. Impressively, the

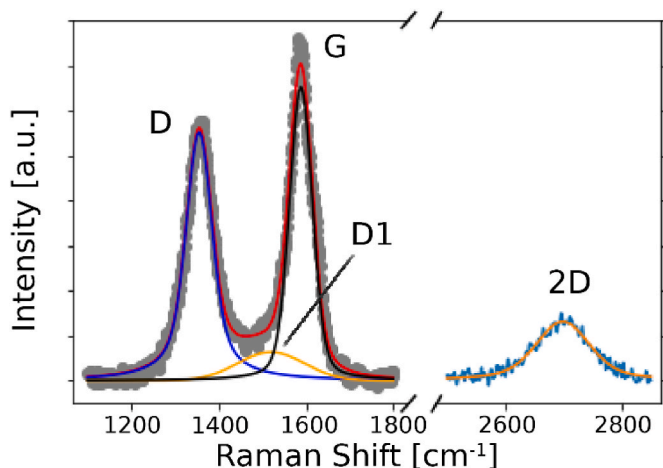
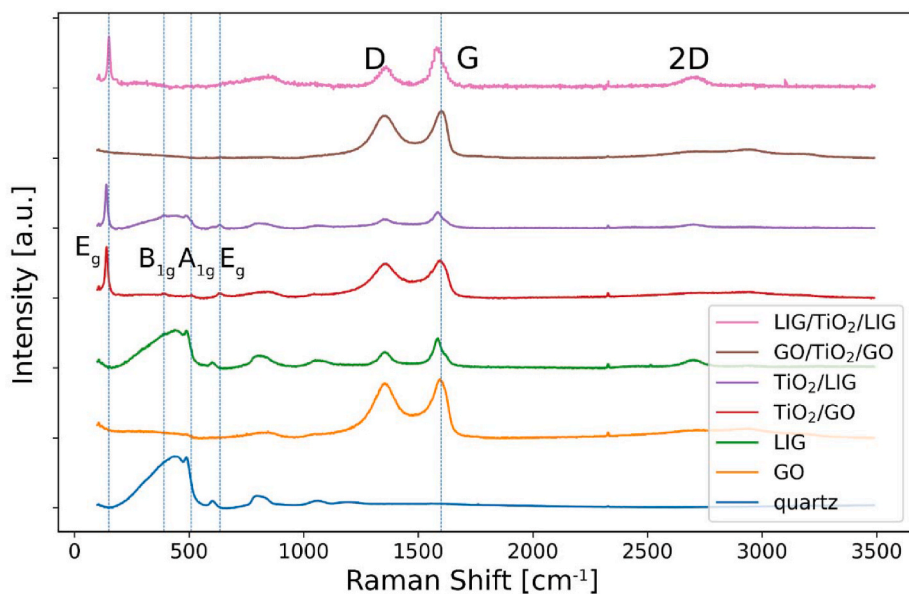
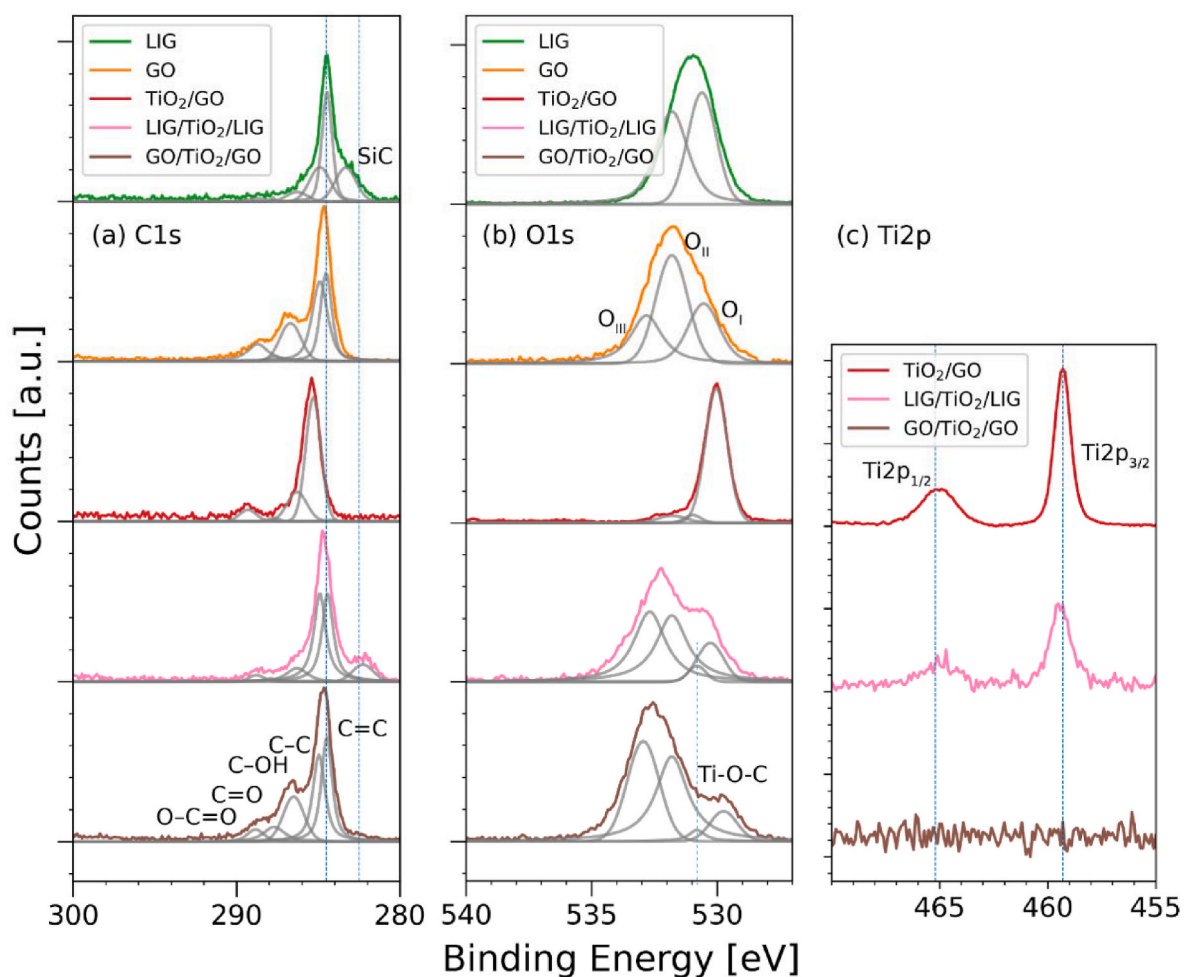


Fig. 2. Raman spectrum characteristic of LIG.



**Fig. 3.** Raman spectra for the layers in the LIG/TiO<sub>2</sub>/LIG capacitor. The TiO<sub>2</sub> anatase bands B<sub>1g</sub>, A<sub>1g</sub>, E<sub>g</sub> are emphasized with the dashed vertical lines. The vertical dashed line at ~1585 cm<sup>-1</sup> is a visual guide to see the structural shift of the G-band from GO to LIG.



**Fig. 4.** High resolution core-level XPS for the LIG/TiO<sub>2</sub>/LIG capacitor layer-by-layer: (a) C 1s (b) O 1s and (c) Ti 2p (peak fitting on Shirley backgrounds).

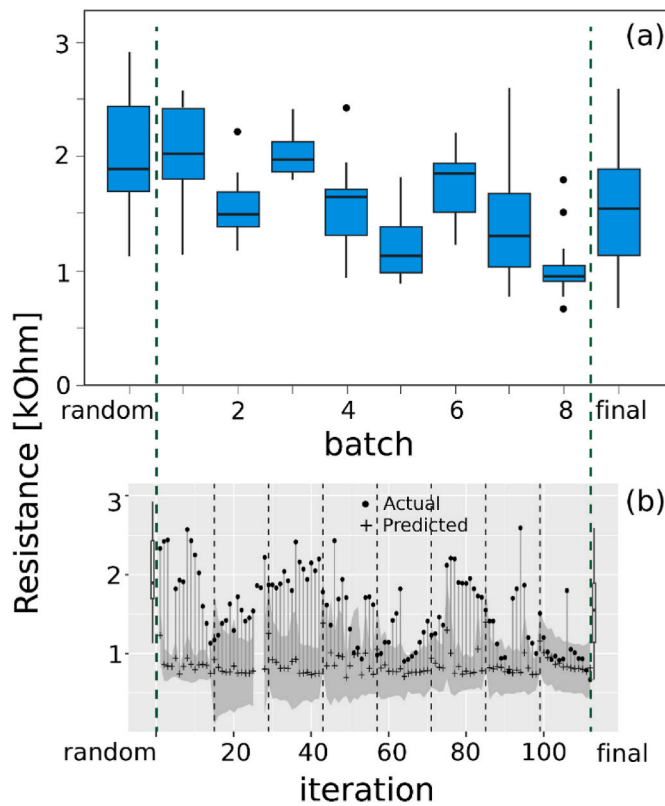


**Fig. 5.** Progress of the optimization of the electrical resistance in produced laser-induced graphene lines, shown in (a) batches and (b) for each iteration within each batch. On the left, the distribution of resistance for the initial training data is shown. The boxplot on the right shows the distribution of measured resistances for all configurations that the BO explored. In (a), each boxplot represents one batch, and each batch consists of 14 lines. In (b), black dashed lines mark the start of the 14 runs in each batch. The gray intervals show the uncertainty of the model for each iteration.

median resistance of the final Bayesian Optimization (BO) batch surpasses the minimum resistance of the initial evaluations, providing conclusive evidence of the effectiveness of our approach. Fig. 5b presents a detailed breakdown of each iterative run, highlighting the associated uncertainties within each batch. Overall, a positive trend in prediction accuracy is observed with each successive batch. As the number of observations increases, the measured resistances consistently align more closely with the predicted values, indicating an improvement in the overall performance of the model.

The minimum resistance overall is comparable to literature (see Table 1); note however that these values are rough estimates as they were compared without consideration of geometry correction factors. It's also noteworthy that, despite the option to parallelize with batches, our experimental setup poses a considerable challenge for Bayesian Optimization. In this context, there's a lack of immediate feedback on the chosen parameter configuration, and as more constant liar evaluations are incorporated, the proposed configurations become

**Table 1**

State-of-the-art literature values for electrical resistance of different LIG materials.

Material	Resistance [kOhm]	Ref
Polyimide	0.3	[59]
GO/SiO <sub>2</sub>	0.25	[34]
GO/nitro-cellulose	2	[60]
SU-8	21	[61]
GO/Au/glass	10	[26]
GO/SiO <sub>2</sub>	0.67	Ours

progressively speculative. Consequently, the experimenter faces a delicate trade-off between the quality of predictions and the number of parallel experiments, a consideration typically tailored to the uniqueness of each experimentation workflow.

We can extract more insights from what the surrogate models have learned using partial dependence plots of a pair of parameters used for the patterning (Fig. 6). Partial dependence plots show how a specific feature's value impacts the predicted outcome of a model while keeping all other features constant. These plots help understand the relationship between individual features and the model's predictions, revealing how changes in one feature influence the model's output. In this study, they indicate that high scanning speeds and mid pressures are generally favorable according to the surrogate model (Fig. 6a). The low- to mid-

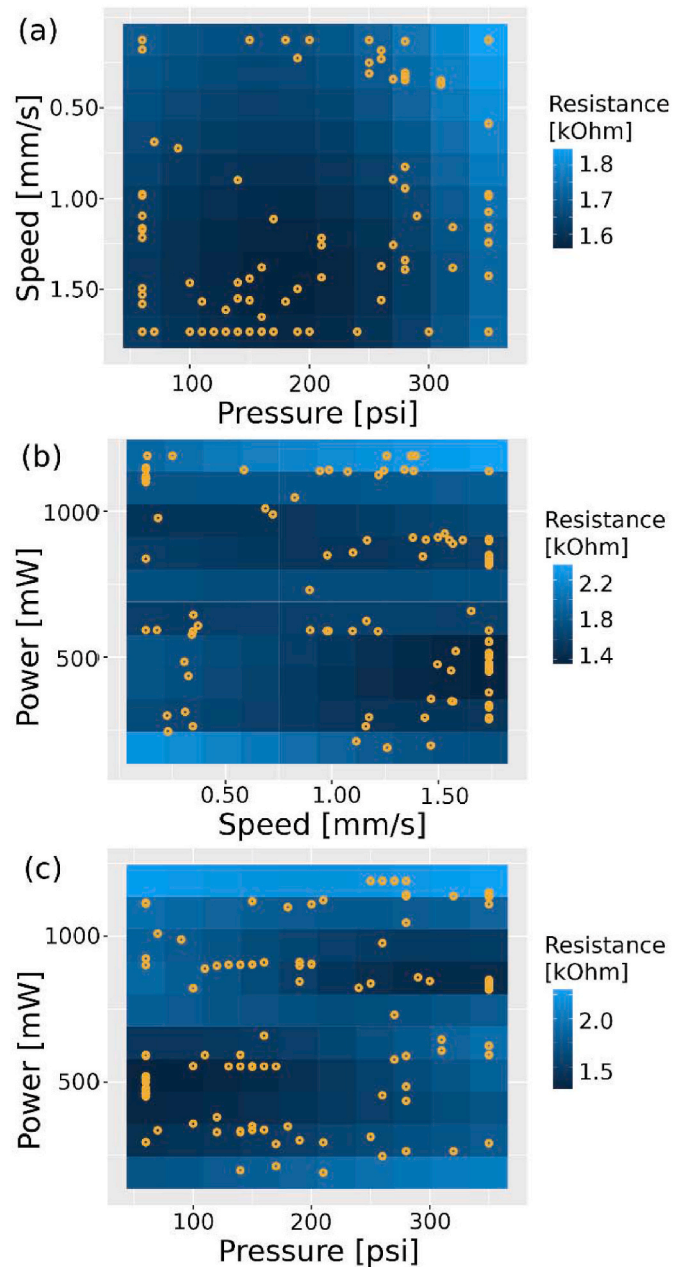


**Fig. 6.** Partial dependence plots for pairs of continuous parameters of the predictions of a surrogate model trained for LIG. Orange circles denote parameter configurations that were evaluated experimentally and are concentrated in the areas with the best predicted electrical resistance. (For interpretation of the references to colour in this figure legend, the reader is referred to the Web version of this article.)

pressure conditions are optimal for plume formations and thermal effects that result in good structural quality [22], and in turn favorable for minimum electrical resistance. Furthermore, low resistance also appears to be achievable at both low and high laser power regions, suggesting that the irradiated power without our parameter design does not play a significant role; although this is in agreement with our previous observations [22], we must note that the reliability of partial dependence estimates can have sampling bias, as shown recently [62]. In particular, well-explored regions show, on average, lower uncertainty than those in less-explored regions. Therefore, a larger experimental evaluation budget can lead to better insights into our surrogate model.

### 3.3. Correlation of structural-electrical properties of laser-induced graphene

The statistically significant correlation between LIG structural parameters and electrical resistance is shown in Table 2 (full table in Table S4). Interestingly, in contrast to our expectations, it is observed that the prominent characteristics of high-quality graphene, i.e. high G/D ratio) is not well correlated to the high conductivity of LIG; instead, the best correlations are found in the set of fitted parameters that are associated with defects-based bands, in particular the D1-band, as evident in Fig. 7a (see also pair plot distributions in Fig. S5). This is complementary to others who report that, for crystalline graphene, electrical resistance decreases with D-peak intensity  $I(D)$  and thus with the number of defects probed by a laser spot [63]. This is in agreement with our observations, albeit less significantly; in contrast, the D1-band shows a stronger trend.

To determine the origins of the D1-band, it is worth comparing the different types of defects that are present. While there are multiple possibilities of where the D1-band originates specifically, we know that it is linked to single-phonon double-resonance defect scattering processes [64], which also give rise to other types of defects e.g. the D2-band convoluted near the G-peak [65]. The correlated D-band observed is activated by vacancies and edge defects [63], which suggests a break in the  $sp^2$  atoms in rings. López-Díaz et al. reported that the width and position of the D1-band in graphene may be indirectly influenced by oxygen content [66]. The experimental data proposes that the removal of oxygen could play a role in restoring the crystallinity of the graphene basal plane. Furthermore, the observed increase in the D1-band has been experimentally associated with a concurrent decline in crystallinity [25,28]. Since the correlation we observed for the D-band is less significant than for the D1-band, this suggests that the patterning process that removed oxygen content whilst preserving the number of  $sp^2$  rings and crystallinity improves the electrical property of LIG.

Our prior study in investigating the high-temperature thermal effects on crystallite sizes of graphene oxide (GO) [40] aligns well with existing literature. Specifically, our study corroborates the observations made by Vollebregt et al. [25] and Claramunt et al. [28], demonstrating that heightened crystallinity corresponds to a decrease in D1-band intensity, and the D1-band width scales accordingly. This relationship underscores the impact of crystallinity on both structural and electrical

**Table 2**

Correlation of fitted Raman peak parameters to the electrical resistance of LIG, as indicated by Spearman coefficient (+1 is perfect positive correlation, -1 is perfect negative correlation; \*\*\*\* $p \leq 1e-4$ , \*\*\* $p \leq 1e-3$ , \*\* $p \leq 1e-2$ , \* $p \leq 5e-2$ ).

variable	correlation	p-value
I(D)	0.379	***
Pos(D)	-0.592	****
Width(D)	0.505	***
I (D1)	0.744	****
Width (D1)	-0.176	*
I(G)	-0.206	*
I (2D/G)	0.348	***

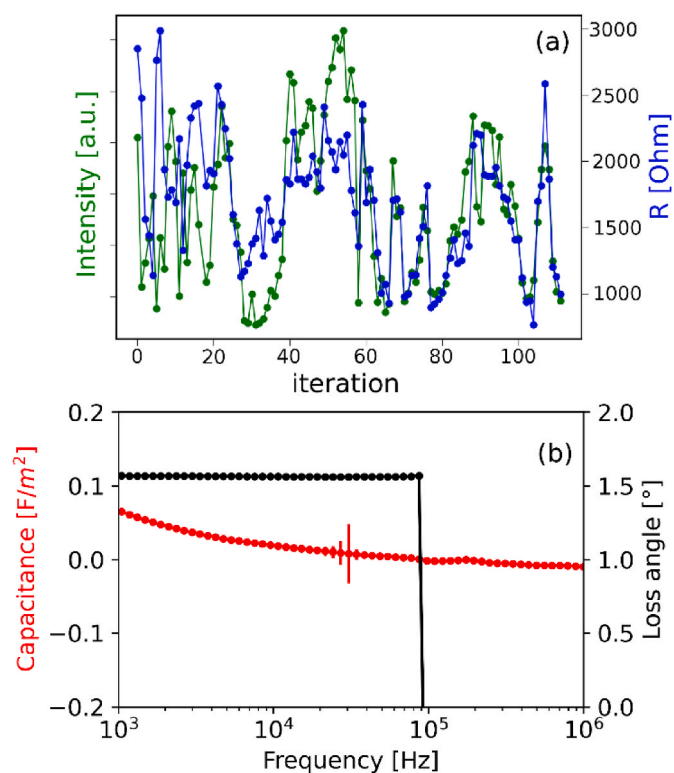


**Fig. 7.** Structural and electrical properties of patterned laser-induced graphene (LIG). (a) Correlation between the Raman D1 structures, which is attributed to amorphous carbon fragments (see Section 3.1) to the electrical resistance; the error bars for both images are removed for clarity; the correlation of all structural peak parameters to electrical resistance is shown in Table S4. (b) The measured capacitance density and the loss angle, averaged over five measurements taken from different patterns on the same sample; the error bars for the loss angle are smaller than the symbol size.

characteristics. Notably, our findings suggest that amorphous phases can serve as electrical charge traps, limiting charge mobility. The notable absence of such phases may be a contributing factor to the observed high electrical conductivity in the material under examination.

The correlations between structural and electrical properties of LIG are also evident in the morphology and the Raman two-dimensional map of the patterned line in Fig. 8. It is interesting to see how the Raman structures depend on the morphology. For the line with the higher resistance (Fig. 8a), higher G/D ratio is found around the edges and not the center of the trenched line. In comparison, the line with lower resistance (Fig. 8b) has a broader and smoother patterned surface, yet the G/D ratio is inhomogeneous throughout. In contrast, the 2D/G map is more clearly homogenous for the more conductive line (Fig. 8b). At first glance, this might be counterintuitive to the trend in Table 2. However, note in Fig. 4a that the electrical resistance is high despite high G/D and 2D/G ratios. Indeed, it seems the structural-electrical correlation is more pronounced with the homogeneity and continuity of the structures. In other words, the prediction of a well-conductive line can be improved with richer and larger input data, i.e. an array of Raman laser spots rather than single spots. Interestingly, the exception to this is the D1-band. The map for the high resistance line in Fig. 8a shows that the D1-band is more present but less homogenous than that for the low-resistance line in Fig. 8b; although the latter map does intuitively demonstrate lower resistance, measuring single spots along the line for Table 2 also show the same trend. Considering the higher cost of measuring two-dimensional maps, this suggests that the structural D1-band is potentially a cheap yet important feature/proxy to predict electrical properties of LIG.

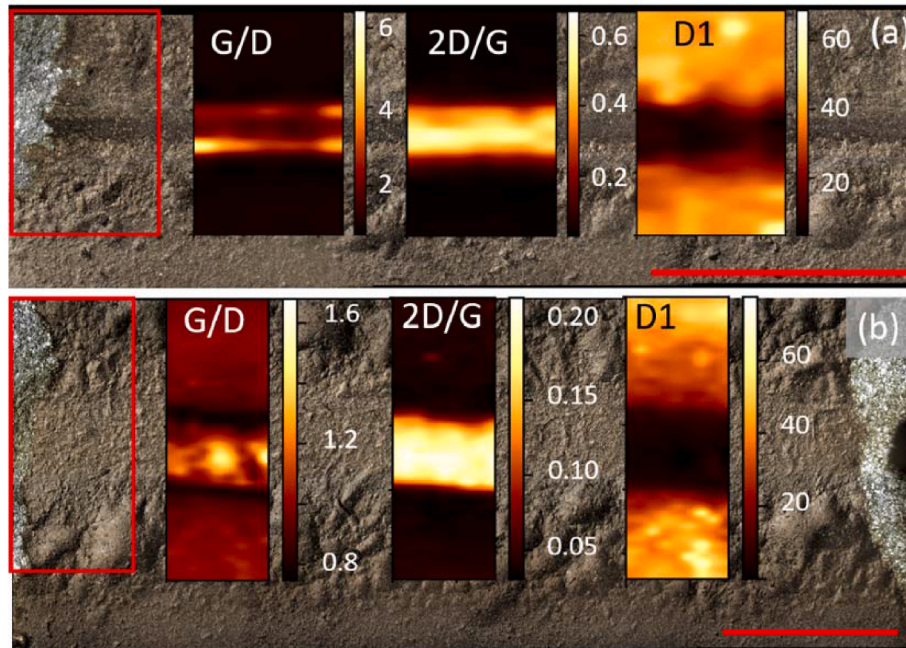


**Fig. 8.** Morphology and Raman two-dimensional map of laser-induced graphene (LIG) with (a) high electrical resistance and (b) low electrical resistance. The bar is 200  $\mu\text{m}$ .

### 3.4. Capacitance-frequency characteristics

The primary focus of characterizing the LIG/TiO<sub>2</sub>/LIG capacitors lies in the frequency-dependent capacitance, which is assessed using an LCR meter to measure the real (R) and imaginary (Z) components of the impedance  $Z = R + iX$ . The formula provided shows the calculation for the loss angle ( $\delta$ ) based on the equivalent circuit of a capacitor in parallel with a resistor:

$$\tan(\delta) = \frac{X}{R} = \frac{1}{\omega C_p R_p}$$

In this context,  $\omega$  represents the angular frequency,  $R_p$  corresponds to the parallel resistance, and  $C_p$  refers to the parallel capacitance. In Fig. 7b, the frequency dependency of the capacitance density  $C_p/A$  and the loss tangent are shown. It is clearly seen that capacitance decreases with increasing frequency. The higher capacitance values at low frequencies have been reported by others as excess capacitance contribution by interface states at the metal-insulator interface, which can follow the low frequency AC signal [67,68]. The capacitance gradually decreases but remains relatively stable between frequencies of about 1 kHz–100 kHz, averaging 9.2 pF and corresponding to a high dielectric constant ( $k \sim 78$ ) commonly found in TiO<sub>2</sub> thin-film capacitors [69,70]. In an ideal capacitor the voltage lags the current by 90°, or a loss angle of 0°. The loss angle is stable around 1.5° close to 0° across the aforementioned frequencies. The gradual decrease in capacitance may be due to the decreased response of the interface states that are unable to follow high frequency input signals [67,68].

Negative capacitance (NC) regions observed at higher frequencies (~100 kHz–1 MHz) generally indicate an inductive behavior in the material. However, there are varying opinions within the research community regarding the nature of the NC phenomenon, depending on the materials and frequency regimes under investigation. Ferroelectric and non-ferroelectric materials exhibit NC originating from distinct sources [71,72]. In some cases, the pseudo NC effect has been observed in high-frequency (MHz) regimes, which is attributed to defect states in the material, such as strain, trap-states, and oxygen vacancies [73,74]. Our XPS results confirm that oxygen vacancies are prevalent structural defects in high permittivity oxides such as TiO<sub>2</sub>. These vacancies have a

direct impact on electrical performance. Hu et al. conducted a study on a single-crystal TiO<sub>2</sub> thin film device, revealing the coexistence of memristive behavior and the NC effect. They explained that the NC effect in this case is attributed to a conductive state change caused by the migration of oxygen vacancies in the TiO<sub>2</sub> thin film [75].

Graphene-based devices have also demonstrated NC effects, with explanations including minority carrier injection into polarization and interface states in Graphene-TiO<sub>2</sub> diodes [76], space charge accumulation in inkjet-printed PANI/reduced GO nanocomposites [20], or surface plasmon resonances in graphene/PPS composites [77]. However, it should be noted that plasmon frequencies typically occur at much higher ranges (10–100 THz) than the frequencies observed in this study (around 100 kHz).

Based on the present work, it is believed that the observed NC effect is likely a combination of two phenomena. Firstly, contact injection strongly influences the small-signal characteristics and results in NC after 100 kHz [76,78]. Secondly, defect states in oxide-based samples play a role [73,74], where localized charge carriers trapped within defect sites gain energy from the externally applied field, particularly at high frequencies. These charge carriers then hop between sites along a nonlinear path, leading to the dominant inductive component and a change in capacitance polarity at approximately 100 kHz.

## 4. Discussion

There are several directions for future research. Firstly, although partial dependence plots have provided insights into our model, they can be misleading if the model is too complex, especially with respect to feature interactions. Future explainable AI systems should quantify the complexity of the model and integrate them into the optimization process [79]. For example, model selection can depend on the reduced interaction strength among features. Notably, relying solely on summarizing these averaged effects with a single numerical value (e.g. averaged coefficient of a linear model) can prove unreliable; for instance, in cases where feature effects exhibit a U-shaped pattern, the average effect might be zero. Consequently, rather than providing one numerical value, it's beneficial to segment a given model and report the coefficients of the segmented model. The partial dependence analysis

conducted in this study marks a crucial initial stride towards integrating physics within machine learning.

Second, while we have achieved good electrical properties, the simultaneous optimization of other objectives, such as the structural and thermal properties, can be beneficial to fabricate electronic devices. Multi-objective optimizations often face the challenge of improving one property at the expense of degrading another. To address this, the concept of a Pareto front, which represents the optimal trade-off between different configurations, is commonly used. However, multi-objective optimization can be data exhaustive [80]. As a result, many materials discovery studies prioritize single-objective optimization, which allows for combining multiple objectives into a single criterion to support multi-objective optimization. Another practical challenge is that often measurements can only be taken at multiple levels. For example, Raman characterization of a material can happen immediately after LIG patterning has been performed, but measurements of electric resistance in this study were performed after an experimental campaign is finished as this requires removal of the sample from the reaction chamber. Our batch optimization approach is a step towards integrating multi-level measurements that occur at different frequencies into a Bayesian optimization process, and would potentially allow further improvements.

Finally, a more comprehensive understanding of the NC phenomenon is needed to fully leverage the unique effects observed in this study and in current literature. These effects include diverging negative/positive capacitance at characteristic resonance frequencies (kHz) and high-frequency (MHz) negative capacitance. Future research can explore machine learning approaches that consider the frequency range in which NC occurs, unlocking opportunities to compensate for parasitic capacitances, reduce power consumption, and extend the operational bandwidth of advanced electronic devices. Additionally, the use of laser direct writing techniques can enhance the feasibility and applicability of these advancements.

## 5. Conclusion

We have demonstrated the application of state-of-the-art automated parameter optimization techniques to laser-induced graphene (LIG) patterning and improved the electrical resistance of LIG patterns. The best LIG resistance was achieved within eight batch configurations suggested by the BO, and is comparable to state-of-the-art values. The initial surrogate models were trained with random parameter evaluations that are independent of the skills and experience of individual researchers – our method does not rely on skilled operators to “guide” it towards good results. Further, our system can optimize material properties for which characterizations are only available outside of the self-driving experiment loop. We further demonstrate how the surrogate model can be used to improve our understanding of the underlying processes for LIG patterned on quartz. The partial dependence analysis identified relevant physical domains for further investigation after optimization, leading to the observance of negative capacitance and a correlation between structural and electrical properties in LIG. This conclusion is supported by XPS, Raman and optical characterizations.

## Declaration of competing interest

The authors declare that they have no known competing financial interests or personal relationships that could have appeared to influence the work reported in this paper.

## Acknowledgements

The authors gratefully acknowledge the financial support by NASA EPSCoR (Grant #80NSSC20M0050), the University of Wyoming's Engineering Initiative of the College of Engineering and Applied Science and the School of Energy Resources.

## Appendix A. Supplementary data

Supplementary data to this article can be found online at <https://doi.org/10.1016/j.ceramint.2023.12.225>.

## References

- [1] J. Lin, Z. Peng, Y. Liu, F. Ruiz-Zepeda, R. Ye, E.L.G. Samuel, M.J. Yacaman, B. I. Yakobson, J.M. Tour, Laser-induced porous graphene films from commercial polymers, *Nat. Commun.* 5 (2014) 1–8, <https://doi.org/10.1038/ncomms6714>.
- [2] J.B. In, B. Hsia, J.-H. Yoo, S. Hyun, C. Carraro, R. Maboudian, C.P. Grigoropoulos, Facile fabrication of flexible all solid-state micro-supercapacitor by direct laser writing of porous carbon in polyimide, *Carbon* 83 (2015) 144–151, <https://doi.org/10.1016/j.carbon.2014.11.017>.
- [3] Z. Peng, J. Lin, R. Ye, E.L.G. Samuel, J.M. Tour, Flexible and stackable laser-induced graphene supercapacitors, *ACS Appl. Mater. Interfaces* 7 (2015) 3414–3419, <https://doi.org/10.1021/am509065d>.
- [4] R. Ye, Z. Peng, T. Wang, Y. Xu, J. Zhang, Y. Li, L.G. Niewski, J. Lin, J.M. Tour, In situ formation of metal oxide nanocrystals embedded in laser-induced graphene, *ACS Nano* 9 (2015) 9244–9251, <https://doi.org/10.1021/acsnano.5b04138>.
- [5] R.A. Fisher, *The Design of Experiments*, Oliver & Boyd, Oxford, England, 1935.
- [6] H. Wahab, J. Gröninger, K. Dickmann, P. Bruns, M. Voß, I. Kardosh, J. Meinschien, L. Aschke, Optimization of laser cutting quality with design of experiments, *Laser Techn. J.* 11 (2014) 27–31, <https://doi.org/10.1002/latj.201400046>.
- [7] R.K. Roy, *A Primer on the Taguchi Method*, Society of Manufacturing Engineers, 1990.
- [8] P. Nikolaev, D. Hooper, F. Webber, R. Rao, K. Decker, M. Krein, J. Poleski, R. Barto, B. Maruyama, Autonomy in materials research: a case study in carbon nanotube growth, *npj Comput. Mater.* 2 (2016) 1–6, <https://doi.org/10.1038/npjcompumats.2016.31>.
- [9] K. Alberi, M.B. Nardelli, A. Zakutayev, L. Mitas, S. Curtarolo, A. Jain, M. Fornari, N. Marzari, I. Takeuchi, M.L. Green, M. Kanatzidis, M.F. Toney, S. Butenko, B. Meredig, S. Lany, U. Kattner, A. Davydov, E.S. Toberer, V. Stevanovic, A. Walsh, N.-G. Park, A. Aspuru-Guzik, D.P. Tabor, J. Nelson, J. Murphy, A. Setlur, J. Gregoire, H. Li, R. Xiao, A. Ludwig, L.W. Martin, A.M. Rappe, S.-H. Wei, J. Perkins, The 2019 materials by design roadmap, *J. Phys. Appl. Phys.* 52 (2018) 1–48, <https://doi.org/10.1088/1361-6463/aad926>.
- [10] S.P. Ong, Accelerating materials science with high-throughput computations and machine learning, *Comput. Mater. Sci.* 161 (2019) 143–150, <https://doi.org/10.1016/j.commatsci.2019.01.013>.
- [11] K. Choudhary, I. Kalish, R. Beams, F. Tavazza, High-throughput identification and characterization of two-dimensional materials using density functional theory, *Sci. Rep.* 7 (2017) 1–16, <https://doi.org/10.1038/s41598-017-05402-0>.
- [12] P.V. Balachandran, A.A. Emery, J.E. Gubernatis, T. Lookman, C. Wolverton, A. Zunger, Predictions of new ABO<sub>3</sub> perovskite compounds by combining machine learning and density functional theory, *Phys. Rev. Mater.* 2 (2018) 1–18, <https://doi.org/10.1103/PhysRevMaterials.2.043802>.
- [13] V. Stanev, C. Oses, A.G. Kusne, E. Rodriguez, J. Pagnione, S. Curtarolo, I. Takeuchi, Machine learning modeling of superconducting critical temperature, *npj Comput. Mater.* 4 (2018) 1–14, <https://doi.org/10.1038/s41524-018-0085-8>.
- [14] O. Isayev, C. Oses, C. Toher, E. Gossett, S. Curtarolo, A. Tropsha, Universal fragment descriptors for predicting properties of inorganic crystals, *Nat. Commun.* 8 (2017) 1–12, <https://doi.org/10.1038/ncomms15679>.
- [15] Z. Hou, Y. Takagiwa, Y. Shinohara, Y. Xu, K. Tsuda, Machine-learning-assisted development and theoretical consideration for the Al<sub>2</sub>Fe<sub>3</sub>Si<sub>3</sub> thermoelectric material, *ACS Appl. Mater. Interfaces* 11 (2019) 11545–11554, <https://doi.org/10.1021/acsaami.9b02381>.
- [16] F. Ren, L. Ward, T. Williams, K.J. Laws, C. Wolverton, J. Hattrick-Simpers, A. Mehta, Accelerated discovery of metallic glasses through iteration of machine learning and high-throughput experiments, *Sci. Adv.* 4 (2018) 1–11, <https://doi.org/10.1126/sciadv.aag1566>.
- [17] Y.K. Wakabayashi, T. Otsuka, Y. Taniyasu, H. Yamamoto, H. Sawada, Improved adaptive sampling method utilizing Gaussian process regression for prediction of spectral peak structures, *APEX* 11 (2018) 1–4, <https://doi.org/10.7567/apex.11.112401>.
- [18] J. Vanschoren, Meta-Learning, *A Survey*, 2018, pp. 1–29, <https://doi.org/10.48550/arXiv.1810.03548>, arXiv, 1810.03548.
- [19] R. Vilalta, Y. Drissi, A perspective view and survey of meta-learning, *Artif. Intell. Rev.* 18 (2002) 77–95, <https://doi.org/10.1023/A:1019956318069>.
- [20] A. Chiolerio, S. Porro, S. Bocchini, Impedance hyperbolicity in inkjet-printed graphene nanocomposites: tunable capacitors for advanced devices, *Adv. Electron. Mater.* 2 (2016) 1500312, <https://doi.org/10.1002/aelm.201500312>.
- [21] D.C. Marcano, D.V. Kosynkin, J.M. Berlin, A. Sinititskii, Z. Sun, A. Slesarev, L. B. Alemany, W. Lu, J.M. Tour, Improved synthesis of graphene oxide, *ACS Nano* 4 (2010) 4806–4814, <https://doi.org/10.1021/nn1006368>.
- [22] H. Wahab, V. Jain, A.S. Tyrrell, M.A. Seas, L. Kothhoff, P.A. Johnson, Machine-learning-assisted fabrication: Bayesian optimization of laser-induced graphene patterning using in-situ Raman analysis, *Carbon* 167 (2020) 609–619, <https://doi.org/10.1016/j.carbon.2020.05.087>.
- [23] A.C. Ferrari, J. Robertson, Interpretation of Raman spectra of disordered and amorphous carbon, *Phys. Rev. B* 61 (2000) 14095–14107, <https://doi.org/10.1103/PhysRevB.61.14095>.
- [24] A.P.M. Leandro, M.A. Seas, K. Vap, A.S. Tyrrell, V. Jain, H. Wahab, P.A. Johnson, Evolution of structural and electrical properties in coal-derived graphene oxide

- nanomaterials during high-temperature annealing, *Diam. Relat. Mater.* 112 (2021) 108244, <https://doi.org/10.1016/j.diamond.2021.108244>.
- [25] S. Vollebregt, R. Ishihara, F.D. Tichelaar, Y. Hou, C.I.M. Beenakker, Influence of the growth temperature on the first and second-order Raman band ratios and widths of carbon nanotubes and fibers, *Carbon* 50 (2012) 3542–3554, <https://doi.org/10.1016/j.carbon.2012.03.026>.
- [26] B. Ma, R.D. Rodriguez, A. Ruban, S. Pavlov, E. Sheremet, The correlation between electrical conductivity and second-order Raman modes of laser-reduced graphene oxide, *Phys. Chem. Chem. Phys.* 21 (2019) 10125–10134, <https://doi.org/10.1039/C9CP00093C>.
- [27] A. Sadezky, H. Muckenhuber, H. Grothe, R. Niessner, U. Pöschl, Raman microspectroscopy of soot and related carbonaceous materials: spectral analysis and structural information, *Carbon* 43 (2005) 1731–1742, <https://doi.org/10.1016/j.carbon.2005.02.018>.
- [28] S. Claramunt, A. Varea, D. López-Díaz, M.M. Velázquez, A. Cornet, A. Cirera, The importance of interbands on the interpretation of the Raman spectrum of graphene oxide, *J. Phys. Chem. C* 119 (2015) 10123–10129, <https://doi.org/10.1021/acs.jpcc.5b01590>.
- [29] R. Saito, M. Hofmann, G. Dresselhaus, A. Jorio, M.S. Dresselhaus, Raman spectroscopy of graphene and carbon nanotubes, *Adv. Phys.* 60 (2011) 413–550, <https://doi.org/10.1080/00018732.2011.582251>.
- [30] X. Dou, I. Hasa, D. Saurel, C. Vaalma, L. Wu, D. Buchholz, D. Bresser, S. Komaba, S. Passerini, Hard carbons for sodium-ion batteries: structure, analysis, sustainability, and electrochemistry, *Mater. Today* 23 (2019) 87–104, <https://doi.org/10.1016/j.matod.2018.12.040>.
- [31] L. Kotthoff, J. Heil, V. Jain, T. Muller, A. Tyrrell, H. Wahab, P.A. Johnson, Optimizing laser-induced graphene production, *Front. Artif. Intell. Appl.* (2022) 31–44.
- [32] P. Getreuer, A survey of Gaussian convolution algorithms, *J. Image Process. Line* 3 (2013) 286–310, <https://doi.org/10.5201/ipol.2013.87>.
- [33] M.C. Biesinger, Accessing the robustness of adventitious carbon for charge referencing (correction) purposes in XPS analysis: insights from a multi-user facility data review, *Appl. Surf. Sci.* 597 (2022) 153681, <https://doi.org/10.1016/j.apsusc.2022.153681>.
- [34] C. Marquez, N. Rodriguez, R. Ruiz, F. Gamiz, Electrical characterization and conductivity optimization of laser reduced graphene oxide on insulator using point-contact methods, *RSC Adv.* 6 (2016) 46231–46237, <https://doi.org/10.1039/C6RA03630A>.
- [35] B. Bischl, R. Sonabend, L. Kotthoff, M. Lang, *Applied Machine Learning Using Mlr3 in R*, CRC Press, 2023.
- [36] L. Schneider, M. Becker, *Advanced tuning methods and black box optimization*, in: B. Bischl, R. Sonabend, L. Kotthoff, M. Lang (Eds.), *Applied Machine Learning Using Mlr3 in R*, CRC Press, 2023.
- [37] D. Ginsbourger, R. Le Riche, L. Carraro, Kriging is well-suited to parallelize optimization, in: Y. Tenne, C.-K. Goh (Eds.), *Computational Intelligence in Expensive Optimization Problems*, Springer Berlin Heidelberg, Berlin, Heidelberg, 2010, pp. 131–162.
- [38] A. Ferrari, J. Robertson, S. Reich, C. Thomsen, Raman spectroscopy of graphite, *Philos. Trans. R. Soc. London, Ser. A: Math. Phys. Eng. Sci.* 362 (2004) 2271–2288, <https://doi.org/10.1098/rsta.2004.1454>.
- [39] L.G. Cançado, A. Jorio, E.H.M. Ferreira, F. Stavale, C.A. Achete, R.B. Capaz, M.V. O. Moutinho, A. Lombardo, T.S. Kulmala, A.C. Ferrari, Quantifying defects in graphene via Raman spectroscopy at different excitation energies, *Nano Lett.* 11 (2011) 3190–3196, <https://doi.org/10.1021/nl201432g>.
- [40] A.P.M. Leandro, M.A. Seas, K. Vap, A.S. Tyrrell, V. Jain, H. Wahab, P.A. Johnson, Evolution of structural and electrical properties in coal-derived graphene oxide nanomaterials during high-temperature annealing, *Diam. Relat. Mater.* 112 (2021) 1–9, <https://doi.org/10.1016/j.diamond.2021.108244>.
- [41] X. Diez-Betriu, S. Álvarez-García, C. Botas, P. Álvarez, J. Sánchez-Marcos, C. Prieto, R. Menéndez, A. de Andrés, Raman spectroscopy for the study of reduction mechanisms and optimization of conductivity in graphene oxide thin films, *J. Mater. Chem. C* 1 (2013) 6905–6912, <https://doi.org/10.1039/C3TC31124D>.
- [42] R.J. Nemanich, S.A. Solin, First- and second-order Raman scattering from finite-size crystals of graphite, *Phys. Rev. B* 20 (1979) 392–401, <https://doi.org/10.1103/PhysRevB.20.392>.
- [43] S. Liu, C. Liu, W. Wang, B. Cheng, J. Yu, Unique photocatalytic oxidation reactivity and selectivity of TiO<sub>2</sub>-graphene nanocomposites, *Nanoscale* 4 (2012) 3193–3200, <https://doi.org/10.1039/C2NR30427A>.
- [44] K.K.H. De Silva, P. Viswanath, V.K. Rao, S. Suzuki, M. Yoshimura, New insight into the characterization of graphene oxide and reduced graphene oxide monolayer flakes on Si-based substrates by optical microscopy and Raman spectroscopy, *J. Phys. Chem. C* 125 (2021) 7791–7798, <https://doi.org/10.1021/acs.jpcc.1c01152>.
- [45] H. Wahab, C. Jansing, H.C. Mertins, J.H. Kim, S.H. Choi, A. Gaupp, H. Timmers, The identification and characterisation of carbonaceous interface layers of graphene using polarisation-dependent X-ray reflectometry, *Carbon* 137 (2018) 252–265, <https://doi.org/10.1016/j.carbon.2018.05.021>.
- [46] S. Schöche, N. Hong, M. Khorasaninejad, A. Ambrosio, E. Orabona, P. Maddalena, F. Capasso, Optical properties of graphene oxide and reduced graphene oxide determined by spectroscopic ellipsometry, *Appl. Surf. Sci.* 421 (2017) 778–782, <https://doi.org/10.1016/j.apsusc.2017.01.035>.
- [47] Z. Wan, S. Wang, B. Haylock, Z. Wu, T.-K. Nguyen, H.-P. Phan, R. Sang, N.-T. Nguyen, D. Thiel, S. Koulikov, A. Trinchi, Y. Gao, M. Lobino, Q. Li, Localized surface plasmon enhanced laser reduction of graphene oxide for wearable strain sensor, *Adv. Mater. Technol.* 6 (2021) 2001191, <https://doi.org/10.1002/admt.202001191>.
- [48] D. Yang, C. Bock, Laser reduced graphene for supercapacitor applications, *J. Power Sources* 337 (2017) 73–81, <https://doi.org/10.1016/j.jpowsour.2016.10.108>.
- [49] A. Bhaumik, J. Narayan, Conversion of p to n-type reduced graphene oxide by laser annealing at room temperature and pressure, *J. Appl. Phys.* 121 (2017), <https://doi.org/10.1063/1.4979211>.
- [50] K. Krishnamoorthy, M. Veerapandian, R. Mohan, S.-J. Kim, Investigation of Raman and photoluminescence studies of reduced graphene oxide sheets, *Appl. Phys. A* 106 (2012) 501–506, <https://doi.org/10.1007/s00339-011-6720-6>.
- [51] J.-C. Dupin, D. Gonbeau, P. Vinatier, A. Levasseur, Systematic XPS studies of metal oxides, hydroxides and peroxides, *Phys. Chem. Chem. Phys.* 2 (2000) 1319–1324, <https://doi.org/10.1039/A908800H>.
- [52] K. Li, J. Xiong, T. Chen, L. Yan, Y. Dai, D. Song, Y. Lv, Z. Zeng, Preparation of TiO<sub>2</sub>/graphene composites by nonionic surfactant strategy and their simulated sunlight and visible light photocatalytic activity towards representative aqueous POPs degradation, *J. Hazard. Mater.* 250–251 (2013) 19–28, <https://doi.org/10.1016/j.jhazmat.2013.01.069>.
- [53] H.L. Ma, J.Y. Yang, Y. Dai, Y.B. Zhang, B. Lu, G.H. Ma, Raman study of phase transformation of TiO<sub>2</sub> rutile single crystal irradiated by infrared femtosecond laser, *Appl. Surf. Sci.* 253 (2007) 7497–7500, <https://doi.org/10.1016/j.apsusc.2007.03.047>.
- [54] H. Liu, S. Liu, Z. Zhang, X. Dong, T. Liu, Hydrothermal etching fabrication of TiO<sub>2</sub>/graphene hollow structures: mutually independent exposed {001} and {101} facets nanocrystals and its synergistic photocatalytic effects, *Sci. Rep.* 6 (2016) 33839, <https://doi.org/10.1038/srep33839>.
- [55] B. Qiu, Y. Zhou, Y. Ma, X. Yang, W. Sheng, M. Xing, J. Zhang, Facile synthesis of the Ti<sup>3+</sup> self-doped TiO<sub>2</sub>-graphene nanosheet composites with enhanced photocatalysis, *Sci. Rep.* 5 (2015) 8591, <https://doi.org/10.1038/srep08591>.
- [56] T. Lu, R. Zhang, C. Hu, F. Chen, S. Duo, Q. Hu, TiO<sub>2</sub>-graphene composites with exposed {001} facets produced by a one-pot solvothermal approach for high performance photocatalyst, *Phys. Chem. Chem. Phys.* 15 (2013) 12963–12970, <https://doi.org/10.1039/C3CP50942G>.
- [57] P. Mohanty, N.C. Mishra, R.J. Choudhary, A. Banerjee, T. Shripathi, N.P. Lalla, S. Annapoorni, C. Rath, Oxygen vacancy induced phase formation and room temperature ferromagnetism in undoped and Co-doped TiO<sub>2</sub> thin films, *J. Phys. Appl. Phys.* 45 (2012) 325301, <https://doi.org/10.1088/0022-3727/45/32/325301>.
- [58] M. Naeem, S.K. Hasanain, M. Kobayashi, Y. Ishida, A. Fujimori, S. Buzby, S.I. Shah, Effect of reducing atmosphere on the magnetism of Zn(1-x)Co(x)O (0 ≤ x ≤ 0.10) nanoparticles, *Nanotechnology* 17 (2006) 2675–2680, <https://doi.org/10.1088/0957-4484/17/10/039>.
- [59] Z. Wang, K.K. Tan, Y.C. Lam, Electrical resistance reduction induced with CO(2) laser single line scan of polyimide, *Micromachines* 12 (2021) 227, <https://doi.org/10.3390/mi12030227>.
- [60] M.G. Bonando, N.M.M. Fernandes, C.C.C. e Silva, C.J.S. de Matos, L.A.M. Saito, *Patterning and tuning the electrical conductivity of graphene oxide films by laser scribing*, in: B.M.C.C.K. Lee, R. Jason Jones (Eds.), *Frontiers in Optics/Laser Science*, Optica Publishing Group, Washington, DC, 2020. FtU2C.1.
- [61] E. Ludvigsen, N.R. Pedersen, X. Zhu, R. Marie, D.M.A. Mackenzie, J. Emnéus, D. H. Petersen, A. Kristensen, S.S. Keller, Selective direct laser writing of pyrolytic carbon microelectrodes in absorber-modified SU-8, *Micromachines* 12 (2021), <https://doi.org/10.3390/mi12050564>.
- [62] J. Moosbauer, J. Herberinger, G. Casalichio, M. Lindauer, B. Bischl, Explaining Hyperparameter Optimization via Partial Dependence Plots, 2022 04820, <https://doi.org/10.48550/arXiv.2111.04820> arXiv, 2111.
- [63] I. Shlimak, A. Haran, E. Zion, T. Havdala, Y. Kaganovskii, A.V. Butenko, L. Wolfson, V. Richter, D. Naveh, A. Sharoni, E. Kogan, M. Kaveh, Raman scattering and electrical resistance of highly disordered graphene, *Phys. Rev. B* 91 (2015) 045414, <https://doi.org/10.1103/PhysRevB.91.045414>.
- [64] R. Saito, A. Jorio, A.G. Souza Filho, G. Dresselhaus, M.S. Dresselhaus, M. A. Pimenta, Probing phonon dispersion relations of graphite by double resonance Raman scattering, *Phys. Rev. Lett.* 88 (2002) 027401, <https://doi.org/10.1103/PhysRevLett.88.027401>.
- [65] A.C. Ferrari, D.M. Basko, Raman spectroscopy as a versatile tool for studying the properties of graphene, *Nat. Nanotechnol.* 8 (2013) 235, <https://doi.org/10.1038/nnano.2013.46>.
- [66] D. López-Díaz, M. López Holgado, J.L. García-Fierro, M.M. Velázquez, Evolution of the Raman spectrum with the chemical composition of graphene oxide, *J. Phys. Chem. C* 121 (2017) 20489–20497, <https://doi.org/10.1021/acs.jpcc.7b06236>.
- [67] S.M. Faraz, M. Mazhar, W. Shah, H. Noor, Z.H. Awan, M.H. Sayyad, Comparative study of impedance spectroscopy and photovoltaic properties of metallic and natural dye based dye sensitized solar cells, *Phys. B Condens. Matter* 602 (2021) 412567, <https://doi.org/10.1016/j.physb.2020.412567>.
- [68] W. Shah, S.M. Faraz, Z.H. Awan, Photovoltaic properties and impedance spectroscopy of dye sensitized solar cells co-sensitized by natural dyes, *Phys. B Condens. Matter* 654 (2023) 414716, <https://doi.org/10.1016/j.physb.2023.414716>.
- [69] F.J. Maier, M. Schneider, J. Schratzenholzer, U. Schmid, Electrical and microstructural characterization of TiO<sub>2</sub> thin films for flexoelectric devices, *J. Phys. Conf.* 1837 (2021) 012009, <https://doi.org/10.1088/1742-6596/1837/1/012009>.
- [70] F.J. Maier, M. Schneider, A. Artemenko, A. Kromka, M. Stöger-Pollach, U. Schmid, Temperature and ambient atmosphere dependent electrical characterization of sputtered IrO<sub>2</sub>/TiO<sub>2</sub>/IrO<sub>2</sub> capacitors, *J. Appl. Phys.* 131 (2022) 095301, <https://doi.org/10.1063/5.0080139>.
- [71] P. Zubko, J.C. Wojdel, M. Hadjimichael, S. Fernandez-Pena, A. Sené, I. Luk'yanchuk, J.-M. Triscone, J. Íñiguez, Negative capacitance in multidomain

- ferroelectric superlattices, *Nature* 534 (2016) 524–528, <https://doi.org/10.1038/nature17659>.
- [72] N. Mazumder, P. Mandal, R. Roy, U.K. Ghorai, S. Saha, K.K. Chattopadhyay, Negative capacitance in ZnO<sub>1-x</sub>Ch<sub>x</sub> (Ch = S, Se, Te): role of localized charge recombination, *J. Appl. Phys.* 121 (2017) 135702, <https://doi.org/10.1063/1.4979689>.
- [73] D. Mitra, S. Bhattacharjee, N. Mazumder, B. Kumar Das, P. Chattopadhyay, K. K. Chattopadhyay, Strain-induced partial phase transition in TiO<sub>2</sub> nanoparticles manifesting frequency dispersive pseudo-inductive switching of capacitance, *Ceram. Int.* 46 (2020) 20437–20447, <https://doi.org/10.1016/j.ceramint.2020.05.138>.
- [74] N. Besra, K. Sardar, N. Mazumder, S. Bhattacharjee, A. Das, B. Das, S. Sarkar, K. K. Chattopadhyay, CH<sub>3</sub>NH<sub>3</sub>PbI<sub>3</sub> as a radio frequency decoupling capacitor: interplay between Maxwell–Wagner polarization and a pseudo inductive response, *J. Phys. Appl. Phys.* 54 (2021) 175105, <https://doi.org/10.1088/1361-6463/abdd66>.
- [75] P. Hu, J.Q. Lu, S.X. Wu, Q.B. Lv, S.W. Li, Coexistence of memristive behaviors and negative capacitance effects in single-crystal TiO<sub>2</sub> thin-film-based devices, *IEEE Electron. Device Lett.* 33 (2012) 890–892, <https://doi.org/10.1109/LED.2012.2191133>.
- [76] M. Yalcin, F. Yakuphanoglu, Voltage and frequency dependence of negative capacitance behavior in a Graphene-TiO<sub>2</sub> nanocomposite photoanode based on quantum dot sensitized solar cells, *Optik* 183 (2019) 1099–1105, <https://doi.org/10.1016/j.ijleo.2019.02.049>.
- [77] G. Fan, G. Shi, H. Ren, Y. Liu, R. Fan, Graphene/polyphenylene sulfide composites for tailorable negative permittivity media by plasmonic oscillation, *Mater. Lett.* 257 (2019) 126683, <https://doi.org/10.1016/j.matlet.2019.126683>.
- [78] M. Ershov, H.C. Liu, L. Li, M. Buchanan, Z.R. Wasilewski, A.K. Jonscher, Negative capacitance effect in semiconductor devices, *IEEE Trans. Electron. Dev.* 45 (1998) 2196–2206, <https://doi.org/10.1109/16.725254>.
- [79] C. Molnar, G. Casalicchio, B. Bischl, Quantifying model complexity via functional decomposition for better post-hoc interpretability, machine learning and knowledge discovery in databases: international workshops of ECML PKDD 2019, in: September 16–20, 2019, Proceedings, Part I, Springer, Würzburg, Germany, 2020, pp. 193–204.
- [80] K. Deb, Multi-objective optimisation using evolutionary algorithms: an introduction, in: L. Wang, A.H.C. Ng, K. Deb (Eds.), *Multi-objective Evolutionary Optimisation for Product Design and Manufacturing*, Springer London, London, 2011, pp. 3–34.